Journal of the Mechanics and Physics of Solids 145 (2020) 104134

Contents lists available at ScienceDirect

Journal of the Mechanics and Physics of Solids

journal homepage: www.elsevier.com/locate/jmps

Standing surface acoustic waves, and the mechanics of acoustic tweezer manipulation of eukaryotic cells

Xiangjun Peng[a,b], Wei He[a,d], Fengxian Xin[a], Guy M. Genin[b,c,*], Tian Jian Lu[d,e,*]

[a] State Key Laboratory for Strength and Vibration of Mechanical Structures, Xi'an Jiaotong University, Xi'an 710049, P.R. China
[b] U.S. National Science Foundation Science and Technology Center for Engineering Mechanobiology, and Department of Biomedical Engineering, Washington University, St. Louis, MO 63130 United States
[c] Bioinspired Engineering and Biomechanics Center (BEBC), Xi'an Jiaotong University, Xi'an 710049, P.R. China
[d] State Key Laboratory of Mechanics and Control of Mechanical Structures, Nanjing University of Aeronautics and Astronautics, Nanjing 210016, P.R. China
[e] Nanjing Center for Multifunctional Lightweight Materials and Structures (MLMS), Nanjing University of Aeronautics and Astronautics, Nanjing 210016, P.R. China

ARTICLE INFO

Article history:
Received 25 May 2020
Revised 20 August 2020
Accepted 29 August 2020
Available online 02 September 2020

Keywords:
Acoustic radiation force
Standing surface acoustic wave
Eukaryotic cell
Cell sorting

ABSTRACT

Manipulation by focused ultrasound is an emerging technology with much promise for non-contact handling of microscale objects. A particularly promising approach for achieving this with living cells involves incorporating standing surface acoustic waves (SSAWs) into a microfluidic device. SSAWs must be tuned to provide the necessary range of acoustic radiation force (ARF), but models enabling this tuning have neglected the mechanics of the cells themselves, treating cells as rigid or homogenous spheres, and have also neglected energy transfer from the substrate to the fluid at the Rayleigh angle. We therefore applied Mie scattering theory to develop a model of the ARF arising from a SSAW impacting an idealized eukaryotic cell in an inviscid fluid. The cell was treated as a three-layered body with a nucleus, cytoplasm, and cortical layer. Results showed strong dependence on cell structures and the Rayleigh angle that can be harnessed to develop novel applications for cell manipulation and sorting. ARF can be tuned using the new model to both push away and pull back a cell towards the sound source. The proposed analytical model provides a foundation for design of microfluidic systems that manipulate and sort cells based upon their mechanical properties.

1. Introduction

Recent advances in non-contact manipulation of single cells by acoustic tweezers have contributed to breakthroughs in biophysics, microbiology, and cell biology (Ozcelik et al., 2018). The sound frequency and pressure of acoustic tweezers must be optimized to avoid damage to cells and tissues (Wiklund, 2012), and to control cell positions precisely (Ozcelik et al., 2018). Standing surface acoustic wave-based (SSAW-based) acoustic tweezers are widely integrated with microfluidics for this purpose (Ding et al., 2013), and 3D (three-dimensional) SSAW acoustic tweezers have been proposed (Guo et al., 2015, 2016). Theoretical analysis of acoustic manipulation with SSAW is crucial for understanding the underlying mechanisms of acoustic tweezers and for refining the technique.

* Corresponding author at: Nanjing University of Aeronautics and Astronautics, State Key Laboratory of Mechanics, Nanjing 210016, P.R. China.
E-mail addresses: genin@wustl.edu (G.M. Genin), tjlu@nuaa.edu.cn (T.J. Lu).

https://doi.org/10.1016/j.jmps.2020.104134
0022-5096/

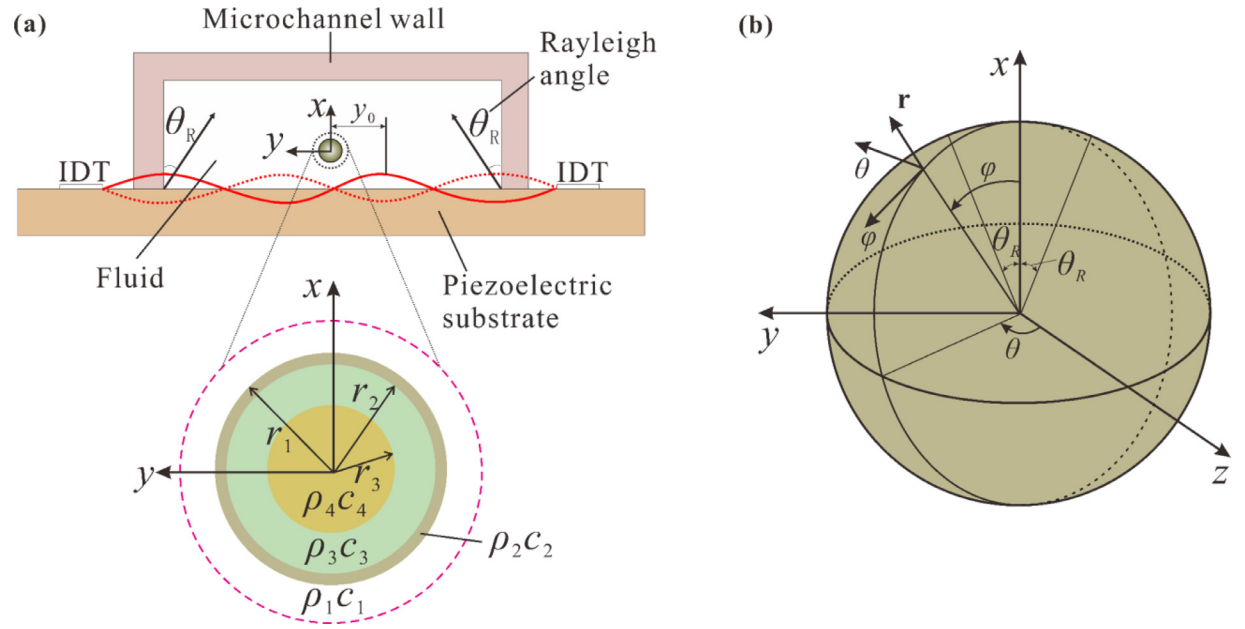

Fig. 1. (a) Schematic of a SSAW incident upon a three-layered model of a eukaryotic cell. (b) The origin of the local spherical coordinate system (r, θ, φ) resides at the instantaneous center of the eukaryotic cell.

Acoustic tweezers operate through control of acoustic radiation force (ARF), a time-averaged, second-order force arising from the scattering of incident waves. To a certain extent, ARF is analogous to the optical radiation force generated by electromagnetic waves impinging upon an electrically or magnetically responsive object (Peng et al., 2017). The large body of literature on the mechanisms and practical applications of ARF begins with Lord Rayleigh's pioneering work on the ARF arising from acoustic waves in compressional fluids (Rayleigh, 1902). Literature relevant to manipulation of cells begins in 1934, when King theoretically calculated the ARF due to a plane wave incident on a small rigid particle surrounded by inviscid fluid (King, 1934). Yosioka and Kawasima extended the theory to elastic spheres, droplets, and gas bubbles by accounting for compressibility of the spherical particle (Yosioka and Kawasima, 1955). Hasegawa further theoretically and experimentally investigated the ARF on solid elastic and viscous spheres, with no restriction placed on the size of the sphere (Hasegawa and Watanabe, 1978; Hasegawa and Yosioka, 1969).

This early work considered only plane incident waves. Recently, other kinds of acoustic beams have been employed to improve the flexibility of acoustic manipulation, including focused Gaussian beams, Bessel beams, cross-plane beams, and SSAWs (Azarpeyvand and Azarpeyvand, 2014; Peng et al., 2020; Xu et al., 2012; Zhang and Zhang, 2012). This includes earlier work from our group demonstrating significant effects of inhomogeneity in acoustic impedance, as can arise with a cell nucleus, on the scattering of a focused, traveling Gaussian ultrasound wave, and on the ARF that such a traveling wave exerts on a cell (Peng et al., 2020). That work identified that, for a simple, traveling waveform, the ARF can be sensitive to cell size. However, such a simplified waveform is applicable only to individual cells and is not practical for biotechnology applications involving cell populations sufficiently large to be of interest physiologically or commercially. The need to identify schemes for ultrasound activation that might be capable of delineating cell sizes in larger cell populations motivated us to develop an entirely new solution based upon more complicated standing (non-traveling) waves in a substantially more advanced device: SSAWs.

However, a theoretical study to establish a foundation for developing this technology has not yet been undertaken (Ding et al., 2013). We therefore undertook such a study with the aim of improving SSAW technologies by revealing the mechanisms underlying acoustic tweezer manipulation of heterogeneous bodies like cells. Conventional theories for estimating ARF are based upon planar standing waves, and therefore fail to consider the transmission of energy from solid to fluid, and the associated influence of the Rayleigh angle, as is needed for the study of surface standing waves (Kim et al., 2019). Moreover, theories for planar standing waves cannot predict the component of ARF acting perpendicular to substrate, as is needed for modeling and controlling particles or cells (Fig. 1a). Generally, a SSAW device consists of two identical interdigital transducers (IDTs) affixed to a piezoelectric substrate, so that the periodic redistribution of charges associated with a periodic electrical signals sent to the IDTs will cause alternating contraction and expansion of the piezoelectric substrate and produce a SSAW (Fig. 1a). When the SSAW contacts the liquid, vibrational energy is transferred as a bulk compressional wave in the liquid, arising at a special refracted angle, the Rayleigh angle, θ_R (Dung Luong and Trung Nguyen, 2010). Therefore, the bulk wave inside the fluid is not always parallel to the piezoelectric substrate.

The components of this bulk compressional wave can sum to a resultant force to that can move a cell relative to the piezoelectric substrate. The first model of this is that of Shen et al. (Liang et al., 2018a), who studied how the Rayleigh angle affects the ARF exerted by a SSAW on an elastic, homogeneous, spherical particle immersed in an inviscid fluid. However, eukaryotic cells typically violate the assumptions of this model because they are inhomogeneous and have nonuniform acoustic impedance, with the nucleus reported to affect wave propagation significantly. Although the model of Shen, et al. has been applied to as a first order estimate of ARF in such situations, this motivated us to extend the model to a more realistic framework for designing acoustical trapping of cells.

We therefore developed a spherically symmetric, three-layered model and calculated the ARF vector induced by a SSAW incident on a three-layered cell using the partial wave expansion method (Fig. 1). Results revealed significant effects of the Rayleigh angle and of the geometrical and acoustic parameters of the nucleus.

2. Theoretical model

SSAWs can be generated by two identical interdigital transducers (IDTs), fabricated on a piezoelectric substrate, that generate two progressive surface acoustic waves traveling towards one other with phase velocity c_s (Fig. 1a). When surface acoustic waves travel along the substrate-fluid boundary, part of the vibrational energy transports into the fluid medium, yielding two compressional waves. Each wave travels with velocity c_f at a Rayleigh angle θ_R (Dung Luong and Trung Nguyen, 2010; Liang et al., 2018a, S. b) with respect to the x-axis:

$$\theta_R = \arcsin\left(c_f/c_s\right) \tag{1}$$

Traveling surface acoustic waves deliver energy from the substrate to the fluid medium, causing wave energy to decay exponentially along the substrate-fluid interface. However, for practical applications based on SSAW, waves are generated in a microchannel sufficiently small relative to the decay length that this attenuation can be neglected in theoretical analysis (Liang et al., 2018a). Therefore, a SSAW can be regarded as two plane progressive waves having identical frequency, phase, and amplitude, and propagating along a certain angle θ_R into the fluid medium.

In a spherical coordinate system (r, θ, φ) with its origin at the instantaneous center of the eukaryotic cell (Fig. 1b), the velocity potential of the incident wave can be expressed as:

$$\begin{aligned}\phi_c &= \phi_0 e^{-i\omega t}\left(e^{i\mathbf{k}_1\cdot(\mathbf{y}_0+\mathbf{r})} + e^{i\mathbf{k}_2\cdot(\mathbf{y}_0+\mathbf{r})}\right)\\ &= \phi_0 e^{-i\omega t}\left(e^{ik_f y_0\sin\theta_R} e^{ik_f r\cos\gamma_1} + e^{-ik_f y_0\sin\theta_R} e^{ik_f r\cos\gamma_2}\right)\\ &= \phi_0 e^{-i\omega t}\sum_{n=0}^{\infty} j_n\left(k_f r\right) X_n\left(\theta,\varphi;k_f y_0,\theta_R\right)\end{aligned} \tag{2}$$

where k_f is the wavenumber of the two surface acoustic waves, γ_1 and γ_2 are the angles between the wave vectors (i.e., $\mathbf{k}_1$ and $\mathbf{k}_2$) and the position vector $\mathbf{r}$, respectively, $j_n(k_f r)$ is the nth order spherical Bessel function of the first kind, and the angular variation function $X_n(\theta, \varphi; k_f y_0, \theta_R)$ is defined in the appendix. Similarly, the velocity potential of the scattered wave is expressed as:

$$\phi_s = \phi_0 e^{-i\omega t}\sum_{n=0}^{\infty} s_n h_n\left(k_f r\right) X_n\left(\theta,\varphi;k_f y_0,\theta_R\right) \tag{3}$$

where s_n is the scattering coefficient and $h_n(k_f r)$ is the nth order spherical Hankel function of the first (outgoing) kind. The total wave field ϕ_1 in the surrounding fluid medium arises from the superposition of the incident and scattered waves, as:

$$\phi_1 = \phi_c + \phi_s \tag{4}$$

A eukaryotic cell suspended in a fluid medium is well approximated by a sphere (Helgason and Miller, 2005). To account for the inhomogeneity of eukaryotic cells, we consider a model of a cell having three layers with different mechanical properties, suspended within a medium of mass density ρ_1 and acoustic velocity c_1. The outermost layer ($r_2 \le r \le r_1$, mass density ρ_2, acoustic velocity c_2) represents a cortical layer that includes the plasma membrane, membrane surface proteins, and cortical actin filaments and contractile myosin motors (Phillips et al., 2012). This layer can range from nanometers for a mesenchymal cell to tens of micrometers for the zona pellucida surrounding an oocyte (Zhang and Cui, 2018). For suspended cells without such a layer, the effect of the nanoscale cortical layer on wave propagation is negligible. The middle layer ($r_3 \le r \le r_2$, mass density ρ_3, acoustic velocity c_3) contains the cellular cytoskeleton and a range of subcellular organelles, lumped into the term "cytoplasm," which we treat as a homogeneous material. Within this is the inner layer ($r \le r_3$, mass density ρ_4, acoustic velocity c_4), a nucleus. The corresponding acoustic impedances and wave numbers are thence $Z_i = \rho_i c_i (i = 1, 2, 3, 4)$ and $k_i = \omega/c_i (i = 1, 2, 3, 4)$, respectively, ω being the circular frequency of incident wave. The velocity potentials ϕ_i in the cortical layer, cytoplasm, and cell nucleus can be expressed directly, as detailed in the Appendix.

The three layers have shear resistance that is small compared to their resistance to dilatation, meaning that they can be approximated as a fluid acoustically (Baddour et al., 2005). The boundary conditions between the layers enforce continuity of normal velocity and normal stress (Fig. 1):

$$\begin{aligned}\mathrm{u}^j\big|_{r=r_j} &= u^{j+1}\big|_{r=r_j}\\ \sigma_{rr}^j\big|_{r=r_j} &= \sigma_{rr}^{j+1}\big|_{r=r_j}\end{aligned} \tag{5}$$

where u^j and $\sigma_{rr}^j (j = 1, 2, 3)$ are the normal velocities and normal stresses in the surrounding fluid medium and the suspended cell, respectively. These quantities can be obtained from the wave fields as:

$$\begin{aligned} u^j &= \frac{\partial \phi_j}{\partial r} \\ \sigma_{rr}^j &= -i\omega \rho_j \phi_j \end{aligned} \tag{6}$$

Incorporating Eq. (6) into Eq. (5) and using Eqs. (2)-(3) and (25)-(27), we can determine the scattering coefficients and then calculate the wave fields.

3. ARF in the *x* direction

For a continuous SSAW travelling in an ideal fluid, the total ARF, **F**, can be determined by integrating the excess of pressure $(p - p_0)$ generated by the sound field over the instantaneous surface $S(t)$ of the eukaryotic cell, as:

$$\mathrm{F} = -\int\int_{S(t)} (p - p_0)\mathrm{n} dS \tag{7}$$

where $\boldsymbol{n}$ is the outward normal to $S(t)$. For proper evaluation of the ARF, the excess of pressure should be taken up to second-order terms in the velocity potential (Hasegawa and Yosioka, 1969). For a periodic wave, the ARF is defined as a time-averaged quantity over period T of the sound field. The time-averaged force acting on a sphere immersed in an infinite ideal fluid is given by:

$$\begin{aligned} \langle \mathrm{F} \rangle = &-\int\int_{S(t)} \langle (p - p_0) \rangle \mathrm{n} dS = -\langle \int\int_{S_0} \rho \langle (u_n \mathrm{n} + u_t \mathrm{t}) u_n \rangle \mathrm{n} dS \rangle \\ &+ \int\int_{S_0} \left[\tfrac{1}{2} \tfrac{\rho}{c^2} \langle \left(\mathrm{Re}\left[\tfrac{\partial \phi_1}{\partial t} \right] \right)^2 \rangle - \tfrac{1}{2} \rho \langle |\nabla \ \mathrm{Re}[\phi_1]|^2 \rangle \right] \mathrm{n} dS \end{aligned} \tag{8}$$

where $\langle \cdot \rangle$ is represents the time average, $\mathbf{t}$ is the outward-pointing unit tangential vector of S, S_0 is the surface of the target at its equilibrium position, $dS = r dr d\theta$, and the parameters $u_n \mathbf{n}$ and $u_t \mathbf{t}$ are the radial and tangential components of the velocity at the surface, respectively.

The ARF generated by the SSAW can be decomposed into two forces pointing in the positive x and y directions. The force in the positive x direction, F_x, can be expressed as:

$$F_x = F_{xnn} + F_{xtt} + F_{xnt} + F_{xt} \tag{9}$$

where:

$$F_{xnn} = -\frac{1}{2} \rho_1 r_1^2 \int_0^{\pi} \int_0^{2\pi} \langle {u_r}^2 \rangle \Big|_{r=r_1} \sin^2\theta \cos\varphi d\varphi d\theta \tag{10}$$

$$F_{xtt} = \frac{1}{2} \rho_1 r_1^2 \int_0^{\pi} \int_0^{2\pi} \langle {u_\theta}^2 + {u_\varphi}^2 \rangle \Big|_{r=r_1} \sin^2\theta \cos\varphi d\varphi d\theta \tag{11}$$

$$F_{xnt} = -\rho_1 r_1^2 \int_0^{\pi} \int_0^{2\pi} \left(\langle u_r u_\theta \rangle \cos\theta \cos\varphi - \langle u_r u_\varphi \rangle \sin\varphi \right) \Big|_{r=r_1} \sin\theta d\varphi d\theta \tag{12}$$

$$F_{xt} = -\frac{\rho_1 r_1^2}{2{c_1}^2} \int_0^{\pi} \int_0^{2\pi} \left\langle \mathrm{Re}\left[\frac{\partial \phi_1}{\partial t} \right]^2 \right\rangle \Big|_{r=r_1} \sin^2\theta \cos\varphi d\varphi d\theta \tag{13}$$

in which u_θ and u_φ are the components of velocity in the surrounding fluid medium pointing towards the polar and azimuthal directions, respectively.

We define the dimensionless ARF in the positive x direction, Y_{px}, as:

$$Y_{px} = F_x / (S_c E) \tag{14}$$

where $S_c = \pi {r_1}^2$ is the cross-sectional area of the entire cell and $E = \frac{1}{2} \rho_1 {k_1}^2 {\phi_0}^2$ is the mean energy density of the incident sound wave. Incorporating Eq. (9) into Eq. (14) and using Eqs. (10)-(13), we can finally obtain the dimensionless ARF as:

$$Y_{px} = -\frac{16}{(k_1 r_1)^2} \sum_{n=0}^{\infty} (\alpha_n + \alpha_{n+1} + 2\alpha_n \alpha_{n+1} + 2\beta_n \beta_{n+1}) D_n(k_1 y_0, \theta_R) \tag{15}$$

where α_n and β_n are the real and imaginary parts of the scattering coefficient s_n, respectively, and

$$\begin{aligned} D_n(k_1 y_0, \theta_R) = &\sum_{m=0}^{n} \begin{bmatrix} \frac{(n-m+1)!}{(n+m+1)!} P_n^{m+1}(0) P_{n+1}^m(0) \\ -\frac{(n-m)!}{(n+m)!} P_n^m(0) P_{n+1}^{m+1}(0) \end{bmatrix} \\ \times &\begin{bmatrix} \cos^2(k_1 y_0 \sin\theta_R) \cos(m+1)\theta_R \cos m\theta_R \\ +\sin^2(k_1 y_0 \sin\theta_R) \sin(m+1)\theta_R \sin m\theta_R \end{bmatrix} \end{aligned} \tag{16}$$

Table 1
Acoustic parameters (Baddour et al., 2005; Mishra et al., 2014; Peng et al., 2020).

Material	Density ρ_i (kg/m^3)	Speed of sound c_i (m/s)	Impedance Z_i (MRayl)
Cortical layer	970	1450	1.41
Cytoplasm	1139	1508	1.72
Nucleus	1430	1508.5	2.16
Water	1000	1500	1.50

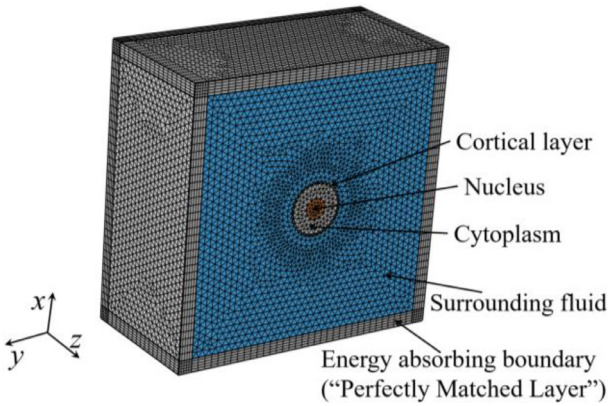

Fig. 2. Representative finite element model for a eukaryotic cell in a fluid medium excited by a piezoelectric device that produces SSAWs.

In Eq. (15), each term is weighted by the factor $D_n(k_1 y_0, \theta_R)$, indicating that the dimensionless ARF is a function of the Rayleigh angle. When the Rayleigh angle is 0°, the wave fronts degenerate into a plane travelling wave in the x direction. In this case, there is no force in the y direction and the proposed theory reduces to the dimensionless ARF for a plane travelling wave. By contrast, when the Rayleigh angle is 90°, the generated wave degenerates into a plane standing wave in the y direction, with no force in the x direction, as can be verified by incorporating $\theta_R = 90^\circ$ into Eq. (16).

The Rayleigh angle θ_R is determined by the speeds of sound in the piezoelectric substrate and the surrounding fluid medium (Eq. (1)). In practical applications, the Rayleigh angle varies over the range of $1.6^\circ - 90^\circ$ (Liang et al., 2018a). When a SSAW is generated on the piezoelectric substrate, its wavelength λ_s and wavenumber k_s are determined by the IDTs. Correspondingly, the wavelength λ_f and wavenumber k_f in the surrounding fluid medium can be expressed as $\lambda_f = \lambda_1 = \lambda_s \sin\theta_R$ and $k_f = k_1 = k_s \sin\theta_R$, respectively. In subsequent numerical calculations, the parameters as listed in Table 1 are used. The relative size of the nucleus varies dramatically amongst animal cells, with the nucleus taking the majority of cell volume in a resting lymphocyte, and a much smaller fraction of volume in a fat cell (Phillips et al., 2012). Further, the radii of cortical layer, r_1, cytoplasm, r_2, and cell nucleus, r_3 are fixed at 15 μm, 14 μm, and 6 μm, respectively.

To validate the theoretical model, finite element simulations were conducted using COMSOL Multiphysics software (COMSOL, Inc., Burlington, MA, USA). Because the SSAW and the cell were both symmetric about the xy plane (Fig. 2), we modeled only half of the system and used symmetrical boundary conditions. The fluid medium was modeled as inviscid, enabling use of the "pressure acoustics" module in COMSOL to model wave propagation. Eq. (2) was used to set the background sound field. Because microchannels are typically fabricated with sound absorptive materials, the outer boundary was modeled with a "perfectly matched layer" (PML) that absorbed all energy that entered. The cell and fluid were discretized as shown in Fig. 2, and convergence studies were performed by mesh refinement to ensure mesh independence for each simulation performed. The edge lengths of all elements were restricted to be smaller than one sixth of the wavelength of the fluid medium. The acoustic pressure field and the velocity fields inside the cell and the surrounding fluid were obtained directly by the finite element simulations, and the ARF was calculated from these numerical results using Eq. (7). A typical simulation reached convergence with 110,000 elements (480,000 degrees of freedom) and required 15 min on a laptop computer.

For illustration, with reference to Fig. 3(a), we consider the effect of the acoustic impedances of the cortical layer and cell nucleus while keeping the position parameter set to $y_0 = \lambda_s/2$, so that the cell is centered at the pressure antinodes; the Rayleigh angle was set to $\theta_R = 20^\circ$ The theoretical and the finite element predictions of the dimensionless ARF Y_{px} were within a few percent for all cases and for acoustic excitation frequencies studied. As the SSAW frequency increases, the curve describing the dimensionless ARF Y_{px} exhibits a series of prominent peaks and dips, due mainly to resonant vibrations of the cell, and the magnitude of the peaks decreases. The presence of either a nucleus or a cortical layer can significantly affect the ARF on the cell, with an especially strong effect of the nucleus. This is due to the strong mismatch in acoustic impedance of the nucleus relative to other components, which results in significantly effect on the scattering field. This is consistent with experiments on backscatter from cells (Baddour and Kolios, 2007).

We next consider the effect of the Rayleigh angle (Fig. 3b), with the cell position again fixed at $y_0 = \lambda_s/2$. The dimensionless ARF Y_{px} is largest at around 32 MHz for all values of the Rayleigh angle below 90° with the magnitude of the peak

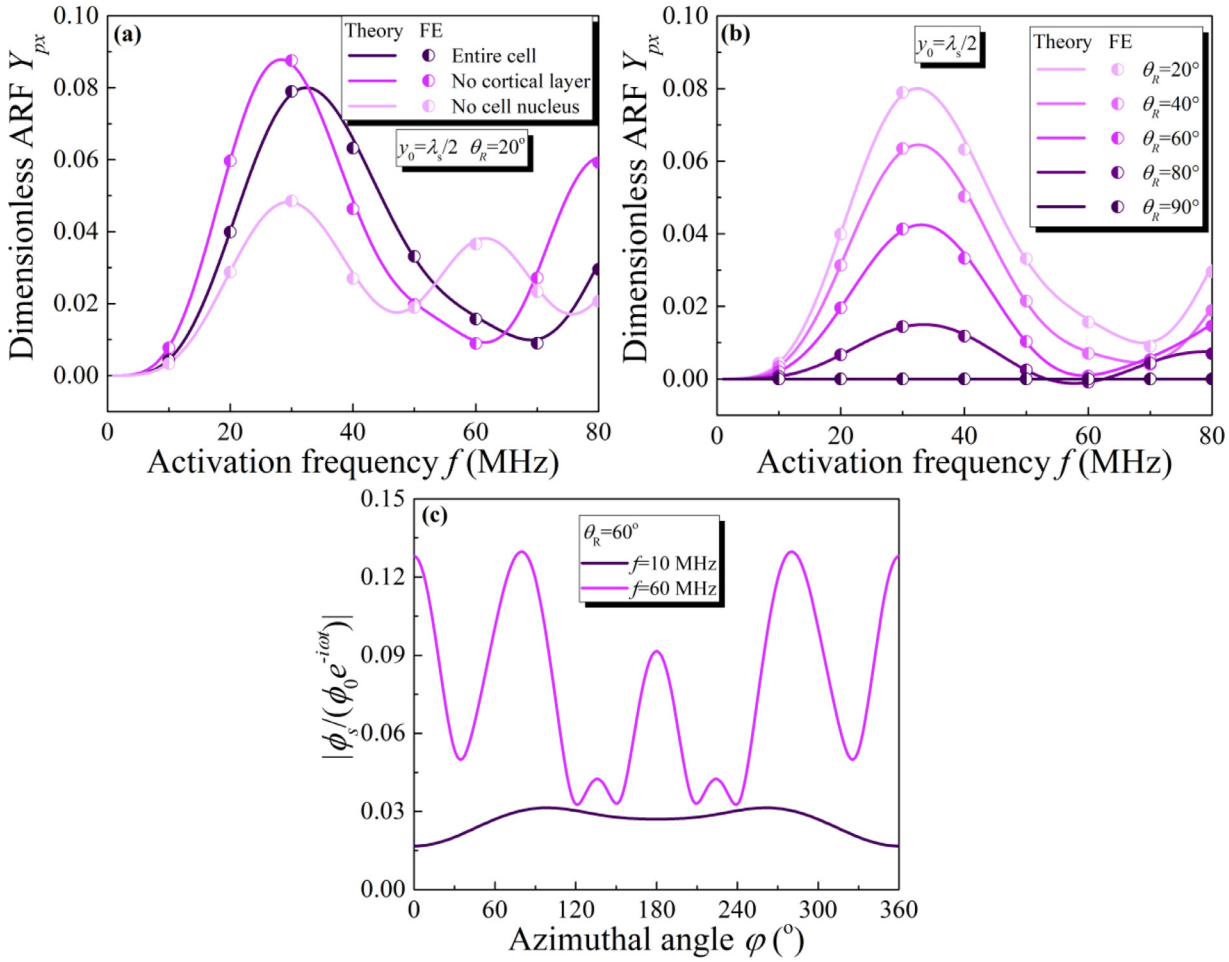

Fig. 3. (a) Dimensionless acoustic radiation force, Y_{px}, versus frequency for an entire cell, a cell lacking a cortical layer, and a cell lacking a nucleus. For the case shown, the cell position parameter is $y_0 = \lambda_s/2$ so that the cell is centered at the pressure antinodes, and the Rayleigh angle is $\theta_R = 20°$ (b) Dimensionless ARF, Y_{px}, versus frequency for an entire cell with several different Rayleigh angles. For the case shown, the position parameter is $y_0 = \lambda_s/2$ so that the cell is centered at the pressure antinodes. For certain frequency ranges at higher Rayleigh angles, the cell is drawn back towards the substrate. (c) Normalized time-independent scattering potential for both the repulsive and attractive behavior are listed with the frequencies being 10 MHz and 60 MHz, respectively. The Rayleigh angle is $\theta_R = 60°$ Symbols: numerical (finite element, FE) simulations; curves: theoretical predictions.

at 32 MHz increasing with decreasing Rayleigh angle. This is expected because more energy will emerge in the x-direction with decreasing Rayleigh angle. This suggests a preferred frequency for manipulating eukaryotic cells when a large ARF is needed. Further inspection of Fig. 3b reveals that Y_{px} can become negative for certain frequencies at larger Rayleigh angles, indicating that the ARF in the x-direction points back towards the substrate.

This attractive force can be understood by considering the scattering potential amplitude, $|\phi_s/(\phi_0 e^{-i\omega t})|$ and considering two excitation frequencies for the case of θ_R =60° and $y_0 = \lambda_s/2$ (Fig. 3c): the case of f=10 MHz, for which the force on the cell is repulsive, and the case of f=60 MHz, for which the force is attractive. Consider the polar angle θ=90° For the case of repulsion (f=10 MHz), $|\phi_s/(\phi_0 e^{-i\omega t})|$ is higher in the hemisphere nearer the substrate(φ=180°) than in the hemisphere further from the substrate (φ=0°), so that the cell is pushed away from the substrate. However, when the opposite occurs, scattering is suppressed in the hemisphere pointing away from the substrate. This occurs at f=60 MHz, and an attractive thus force arises at this frequency, pushing the cell back towards the substrate. This phenomenon is analogous to effects that can arise on a sphere illuminated by a Bessel beam (Marston, 2006), and is meaningful in that enables design of SSAW based acoustic tweezers that can push, trap, or pull back a eukaryotic cell toward the substrate.

The Rayleigh angle is a function of the acoustic wave phase velocity in both the fluid and on the surface of the piezoelectric substrate (cf. Eq. (1)). As such, it is a factor that can be controlled to a degree in the design of such an acoustic trapping or sorting system. Although the range of fluid phase velocity is limited somewhat by the need to grow cells in a nutritional medium, with a sound velocity on the order of $c_f \approx$ 1500 m/s, the range of piezoelectric substrata available enables substantial tunability. For example, the surface wave velocity of $Bi_{12}GeO_{20}$ is $c_s \approx$ 1680 m/s (Pratt et al., 1972), for Rayleigh angle of θ_R= 63.2°, while that of $LiNbO_3$ is $c_s \approx$ 3960 m/s (Holm et al., 1996), for θ_R=22.3°

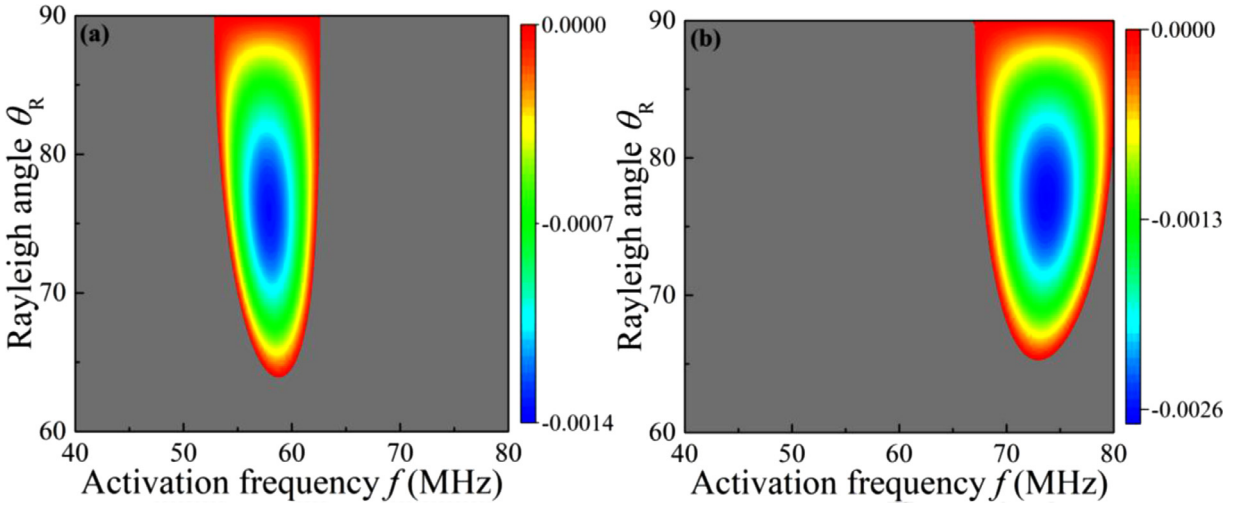

Fig. 4. Contour plots of negative values of the dimensionless ARF, Y_{px}, for (a) pressure antinodes ($y_0 = \lambda_s/2$) and (b) pressure nodes ($y_0 = \lambda_s/4$). Over the majority of parameter space (gray space), Y_{px} is positive and the cell is predicted to be pushed away from the substrate.

For cells with the parameters adopted here, a Rayleigh angle of 22.3° in a $LiNbO_3$ substrate will result in a repulsive force on the cell in x-direction. By tuning this repulsive force with buoyancy and gravity, a cell can be levitated. For a $Bi_{12}GeO_{20}$ substrate (θ_R= 63.2°), Y_{px} is substantially smaller but still negative (Fig. 3b). Here, the attractive force works with gravity and against buoyancy, and can be used with denser nutrition medium to levitate cells. The range of available piezoelectric materials thus enables design of acoustic tweezer devices that can push, trap, or pull back a eukaryotic cell toward the substrate.

To assess the combinations of excitation frequency and Rayleigh angle that induce an attractive (negative) ARF, Y_{px} on an entire cell was calculated over a broad parameter space ($40 \le f \le 80$ MHz and $60^\circ \le \theta_R \le 90^\circ$). Plotting contour plots of negative values of Y_{px} for pressure antinodes ($y_0 = \lambda_s/2$, Fig. 4a) and pressure nodes ($y_0 = \lambda_s/4$, Fig. 4b) revealed that over the majority of parameter space (blank space, Fig. 4), Y_{px} is positive and the cell is predicted to be pushed away from the substrate. Comparing the two panels of Fig. 4 reveals no overlapping regions of attractive force for the two different values of y_0 (colored regions, Fig. 4), meaning that the excitation conditions must be tuned to provide steady attractive force, and that y_0 may be varied to modulate attraction and repulsion by SSAW-based acoustic tweezers.

The variation of ARF with horizontal position y_0 is examined by considering in detail the case of a single wavelength, $\lambda_s = 100\ \mu$m (Fig. 5a). Y_{px} varies strongly with cell position y_0, showing a periodic dependence with a period of the wavelength ($\lambda_s/2$). This periodicity, which is independent of the Rayleigh angle, arises from interference. The amplitude of the dependence increases by orders of magnitude with decreasing Rayleigh angle θ_R (Fig. 5a).

Inspection of the results shown in Fig. 5b provides further insight into the influence of θ_R on the dimensionless ARF Y_{px}. For a three-layered cell located at the pressure antinodes ($y_0 = \lambda_s/2$), there exists a threshold value of θ_R that depends upon λ_s, beyond which Y_{px} drops monotonically due to the weighting factor D_n in Eq. (15). This threshold decreases with increasing wavelength. This is because that changing the Rayleigh angle θ_R here actually changes the frequency in the extracellular fluid. For $\lambda_s = 120\ \mu$m, when the Rayleigh angle θ_R ranges from 30° to 90°, the frequency in extracellular fluid ranges from 25 to 12.5 MHz. In this range, the dimensionless ARF Y_{px} will decrease monotonically, corresponding with Fig. 3b. When the Rayleigh angle θ_R ranges from 1.6° to 30°, the frequency in extracellular fluid ranges from 448 to 25 MHz, respectively. Multiple natural frequencies of the eukaryotic cell will fall into this range and show multiple peaks and dips (Fig. 5b). However, due to the weighting factor D_n in Eq. (15), the dimensionless ARF Y_{px} will become smaller when the Rayleigh angle θ_R increase.

The dimensionless position $k_1 y_0$ determines the effect of Rayleigh angle on ARF (Fig. 5c, for y_0 fixed at $y_0 = 100$ μm). Although changing the Rayleigh angle will not change the extracellular frequency in the fluid, the sensitivity to Rayleigh angle increases with $k_1 y_0$. This is not due to resonance of the cell. Mathematically, larger $k_1 y_0$ means a smaller circle for the trigonometric functions $\cos^2(k_1 y_0 \sin\theta_R)$ and $\sin^2(k_1 y_0 \sin\theta_R)$ in $D_n(k_1 y_0, \theta_R)$. Physically, changing the Rayleigh angle will change the wavelength of the travelling surface acoustic wave λ_s in this case. Since $y_0 = 100\ \mu$m is held constant in Fig. 5c, the distance between the cell center to the antinode could be several times the period of the wavelength ($\lambda_s/2$) as Fig. 5a shows, leading to multiple peaks and dips. The magnitude of the dimensionless ARF Y_{px} decreases with increasing Rayleigh angle as less energy propagates in the x-direction as the Rayleigh angle increases.

For focused ultrasound, the contrast in acoustic impedance due to the nucleus of a cell has a strong effect on the ARF (Peng et al., 2020). We therefore next asked two questions about the role of absolute and relative size of the nucleus. For self-similar cells of different size but with the same relative cortical layer and nucleus sizes ($r_2 = 14r_1/15$ and $r_3 =$

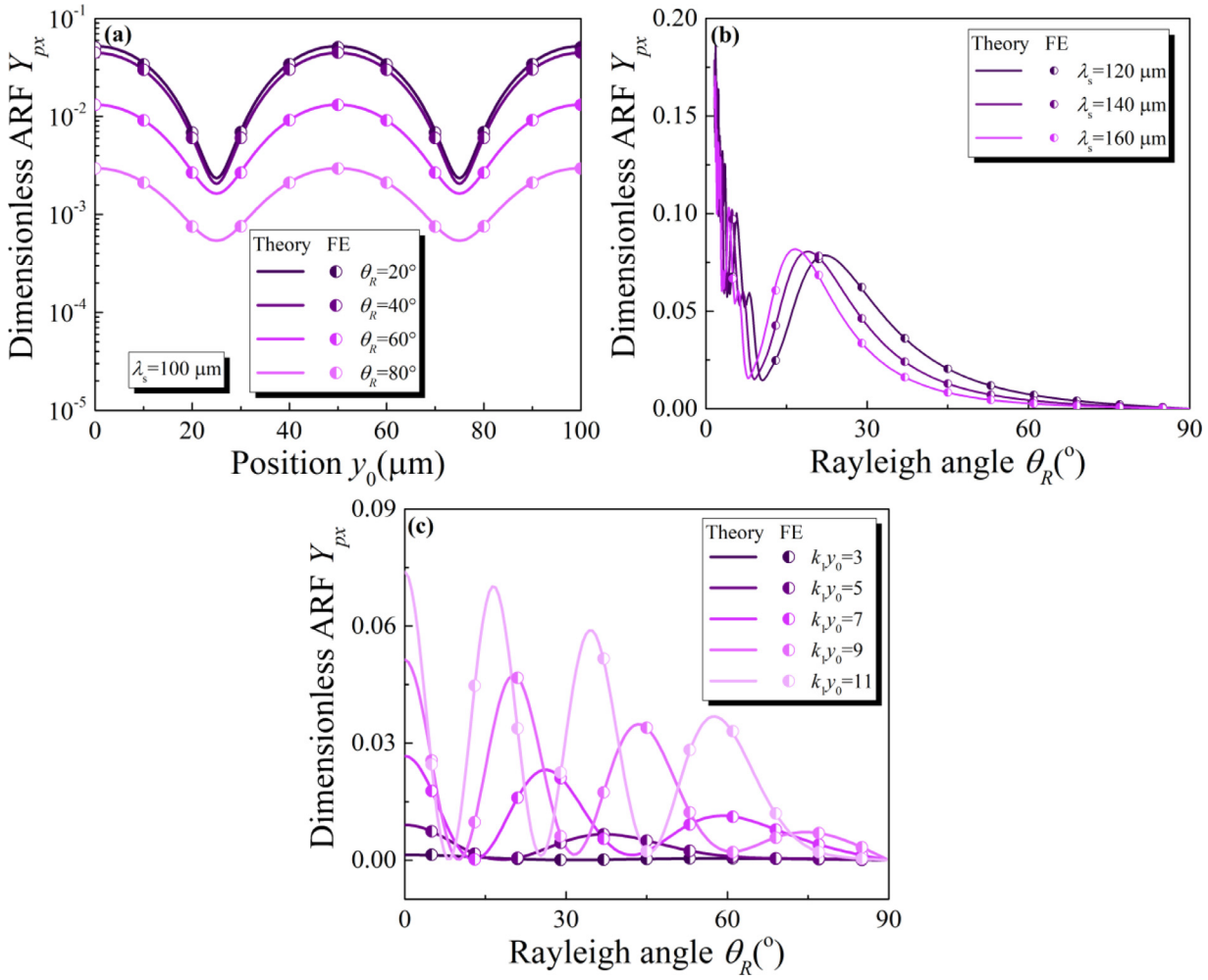

Fig. 5. (a) Dimensionless ARF Y_{px} plotted as a function of y_0 for selected Rayleigh angles, with wavelength λ_s= 100 μm. (b) The dimensionless ARF, Y_{px}, is a strong function of the Rayleigh angle θ_R and the wavenumber (and hence wavelength), as is evident from Eqs. (15)-(16). (c) Dimensionless ARF Y_{px} plotted as a function of Rayleigh angle θ_R for selected k_1y_0. Symbols: numerical (finite element, FE) simulations; curves: theoretical predictions.

$6r_1/15$), the ARF peak shifted to a higher frequency as cell size decreased, while the magnitude of this force peak remained constant (Fig. 6a, with $\theta_R = 20^\circ$ and $y_0 = 0$). For the cases studied, the resonant frequencies all shifted to lower values with increasing cell size. The effects of cell size could be further understood by considering the backscattering amplitude ($\varphi = 180^\circ$, $\theta = 90^\circ$) of the scattered wave, which follows to form: Faran, 1951

$$f_n(f,\theta,\varphi)|_{\theta=90^\circ,\ \varphi=180^\circ} = \frac{2}{k_1 r_1}\sum_{n=0}^{\infty} i^{-n} s_n X_n\left(\theta = 90^\circ,\ \varphi = 180^\circ; k_f y_0, \theta_R\right) \tag{17}$$

Correspondingly, as the size of the cell increased, the peak of the backscattering amplitude $f_n(f, 90^\circ, 180^\circ)$ shifted to a lower frequency without significant change in backscattering amplitude. As a result of this shift, more resonant frequencies and associated peaks appeared for larger cells over the frequency range studied (Fig. 6b). Based on these theoretical results, for smaller cells of radius 10–15μm, increasing the frequency or the sound pressure of the SSAW leads to larger ARF.

The second question relates to how much the ARF changes over the cell cycle, in which the nuclear size stays similar but the cell volume can change substantially. Here, we held the cortical thickness and nuclear radius constant while increasing the cell volume. The ARF peak shifted to a lower frequency and the magnitude of force peaks decreased with increasing cell size (Fig. 6c), different from the self-similar cell case. To further understand the cell size effect, we could also check the backscattering wave with Eq. (17). Correspondingly, as the size of the cell increased, the peak of the backscattering amplitude $f_n(f, 90^\circ, 180^\circ)$ shifted to a lower frequency and lower amplitude. Comparing the results in Fig. 6a and Fig. 6c, we observe that for larger cells, the amplitude of the dimensionless ARF Y_{px} in Fig. 6a was larger than the counterpart in Fig. 6c, while for smaller cells, the converse was true as expected because of the larger nuclear size in Fig. 6a and the dominant role of the elevated acoustic impedance of the cell nucleus.

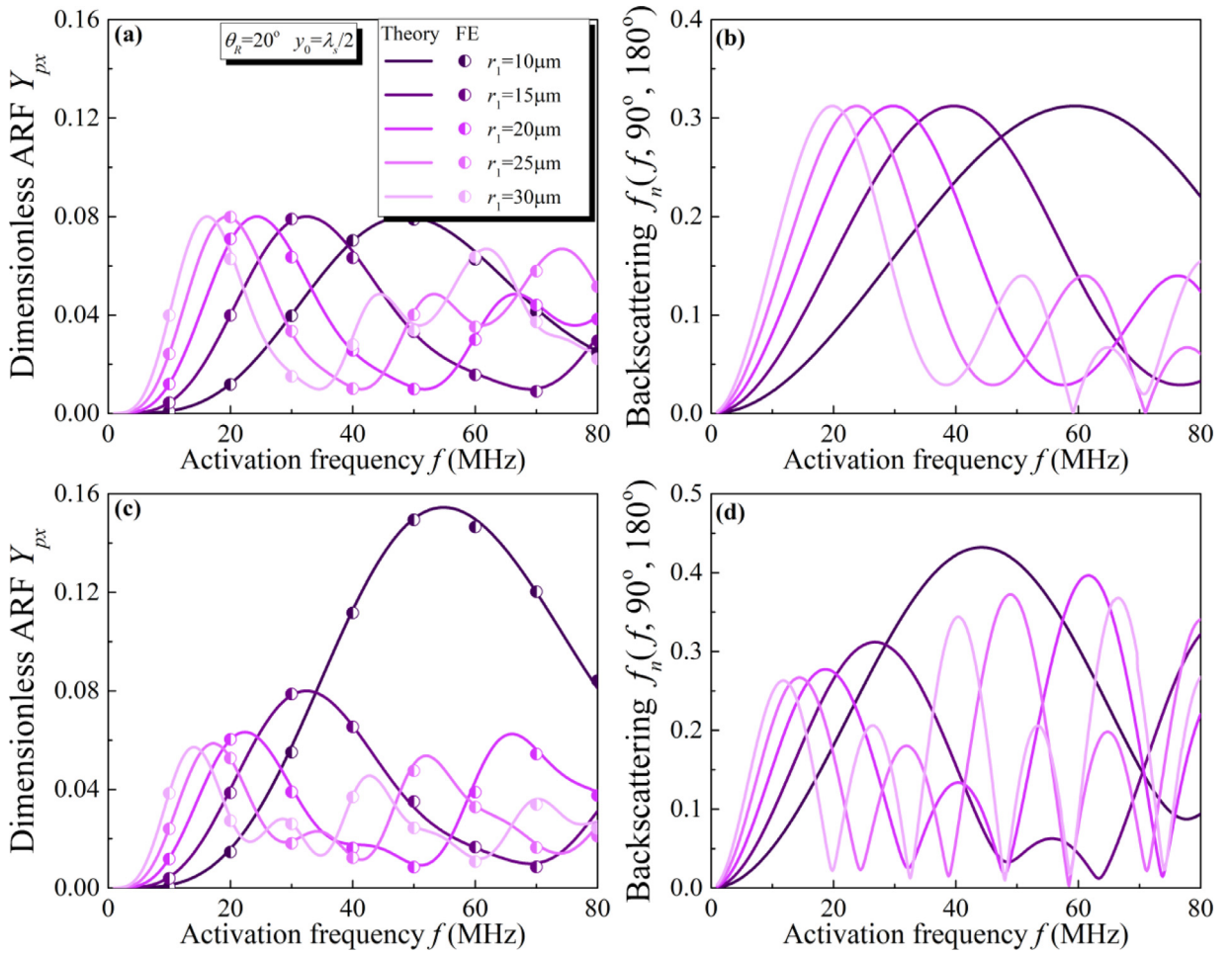

Fig. 6. (a) Dimensionless ARF Y_{px} and (b) backscattering amplitude as a function of frequency for selected values of cell radius (eukaryotic cell immersed in water); here, cells are self-similar, with layer sizes scaling with cell size ($r_2 = 14r_1/15$ and $r_3 = 6r_1/15$, $\theta_R = 20°$ and $y_0 = \lambda_s/2$). (c) Dimensionless ARF Y_{px} and (d) backscattering amplitude for identical cells, but now with the nuclear and cortical layer sizes held constant to represent changes in volume associated with the cell cycle. Here, the thickness of the outer layer $l = r_1 - r_2 = 1\mu$m, the nuclear radius is $r_3 = 6\mu$m, $\theta_R = 20°$ and $y_0 = \lambda_s/2$. Symbols: numerical (finite element, FE) simulations; curves: theoretical predictions.

4. ARF in the *y* direction

Acoustic tweezers additionally require control in planes parallel to the actuator, denoted in our model as the *y*-direction. This force, F_y consists of four terms:

$$F_y = F_{ynn} + F_{ytt} + F_{ynt} + F_{yt} \tag{18}$$

where

$$F_{ynn} = -\frac{1}{2}\rho_1 r_1^2 \int_0^{\pi}\int_0^{2\pi} \langle {u_r}^2\rangle|_{r=r_1} \sin^2\varphi \sin\theta d\theta d\varphi \tag{19}$$

$$F_{ytt} = \frac{1}{2}\rho_1 r_1^2 \int_0^{\pi}\int_0^{2\pi} \langle {u_\theta}^2 + {u_\varphi}^2\rangle|_{r=r_1} \sin^2\varphi \sin\theta d\theta d\varphi \tag{20}$$

$$F_{ynt} = -\rho_1 r_1^2 \int_0^{\pi}\int_0^{2\pi} \left(\langle u_r u_\theta\rangle \cos\varphi \sin\theta + \langle u_r u_\varphi\rangle \cos\theta\right)|_{r=r_1} \sin\varphi d\theta d\varphi \tag{21}$$

$$F_{yt} = -\frac{\rho_1 r_1^2}{2{c_1}^2} \int_0^{\pi}\int_0^{2\pi} \langle \mathrm{Re}\left[\frac{\partial \phi_1}{\partial t}\right]^2\rangle|_{r=r_1} \sin^2\varphi \sin\theta d\theta d\varphi \tag{22}$$

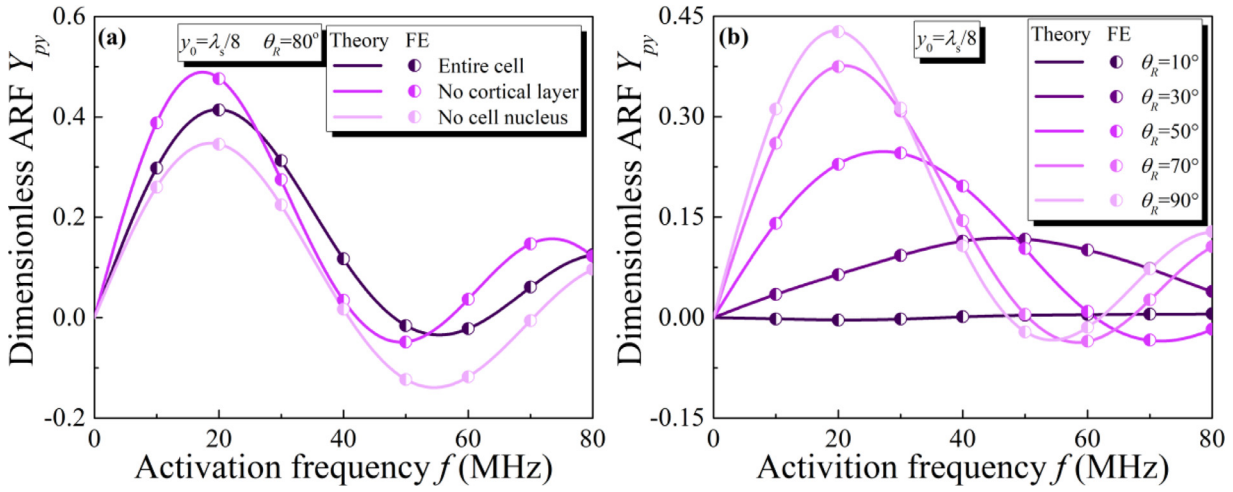

Fig. 7. Dimensionless in-plane ARF versus frequency of an entire cell, a cell lacking a cortical layer, and a cell lacking a nucleus. Position $y_0 = \lambda_s/8$ and Rayleigh angle $\theta_R = 80^\circ$ (b) Dimensionless in-plane ARF, Y_{py}, versus frequency for an entire cell with several different Rayleigh angles. For the case shown, the position parameter is $y_0=\lambda_s/8$. Symbols: numerical (finite element, FE) simulations; curves: theoretical predictions.

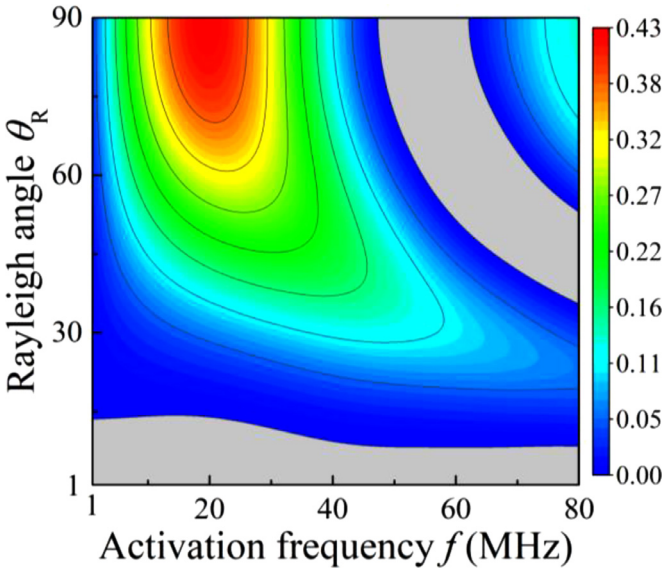

Fig. 8. Conditions for and magnitudes of in-plane, attractive values of the dimensionless ARF Y_{py} for a cell located at $y_0 = \lambda_s/8$ for $1 \le f \le 80$MHz and $1^\circ \le \theta_R \le 90^\circ$.

Normalizing as above so that $F_y = Y_{py} S_c E$, the dimensionless radiation force Y_{py} is:

$$Y_{py} = \frac{8}{(k_1 r_1)^2} \sum_{n=0}^{\infty} (\beta_n - \beta_{n+1} - 2\alpha_n \beta_{n+1} + 2\beta_n \alpha_{n+1}) E_n(k_1 y_0, \theta_R) \tag{23}$$

where

$$E_n(k_1 y_0, \theta_R) = \sum_{m=0}^{n} \sin(2k_1 y_0 \sin\theta_R) \sin(2m+1)\theta_R \times \begin{bmatrix} \frac{(n-m)!}{(n+m)!} P_n^m(0) P_{n+1}^{m+1}(0) \\ -\frac{(n-m+1)!}{(n+m+1)!} P_n^{m+1}(0) P_{n+1}^m(0) \end{bmatrix} \tag{24}$$

As above, Y_{py} is a function of θ_R because of the function $E_n(k_1 y_0, \theta_R)$. When $\theta_R = 0^\circ$, the SSAW is a plane travelling wave in the x-direction that generates no force on the entire cell in the y-direction, as is evident from the fact that $E_n(k_1 y_0, \theta_R)$ is zero for $\theta_R = 0^\circ$, and hence Y_{py} equals zero. When $\theta_R = 90^\circ$, the SSAW degenerates into a plane standing wave, and we recover the Hasegawa solution for a plane standing wave (Hasegawa, 1979) upon substituting $\theta_R = 90^\circ$ into Eq. (23).

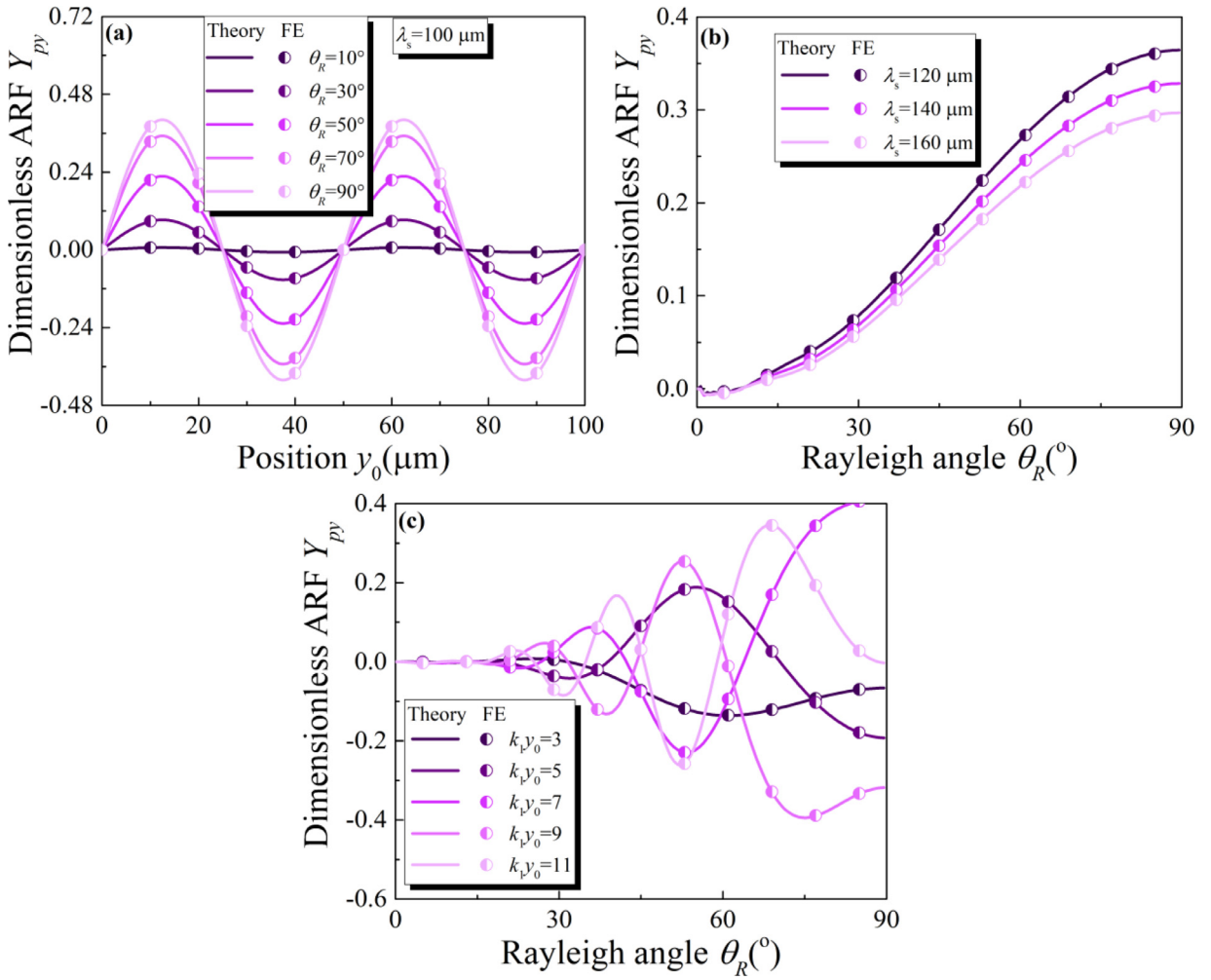

Fig. 9. (a) Dimensionless in-plane ARF Y_{py} plotted as a function of y_0 for selected Rayleigh angles, with wavelength fixed at λ_s= 100 μm. (b) Dimensionless in-plane ARF Y_{py} plotted as a function of Rayleigh angle θ_R for three different wavelengths, with $y_0 = \lambda_s/8$. (c) Dimensionless in-plane ARF Y_{py} plotted as a function of k_1y_0. Symbols: numerical (finite element, FE) simulations; curves: theoretical predictions.

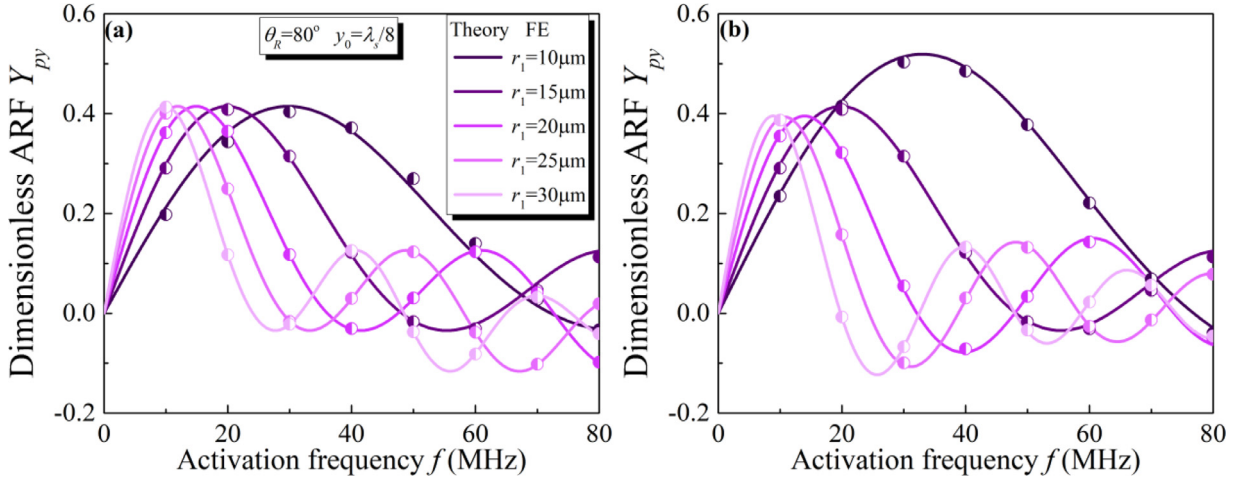

Fig. 10. (a) Dimensionless in-plane ARF Y_{py} plotted as a function of frequency for selected values of cell radius, with $r_2 = 14r_1/15$, $r_3 = 6r_1/15$, $\theta_R = 80^\circ$, and $y_0 = \lambda_s/8$. (b) Dimensionless in-plane ARF Y_{py} plotted as a function of a cell circle, but now with the nuclear and cortical layer sizes held constant to represent changes in volume associated with the cell cycle. Here, the thickness of the outer layer $l = r_1 - r_2 = 1\mu$m, the nuclear radius is $r_3 = 6\mu$m, $\theta_R = 80^\circ$ and $y_0 = \lambda_s/8$. Symbols: numerical (finite element, FE) simulations; curves: theoretical predictions.

Cell structure affects Y_{py}, with the nucleus playing an especially important role (Fig. 7, with position $y_0 = \lambda_s/8$ and Rayleigh angle $\theta_R = 80^\circ$). The sign of the ARF (attractive versus repulsive) can be changed in this plane as well by adjusting the excitation frequency (Fig. 7a). Note the trend for Y_{py} is opposite that for Y_{px} in Fig. 3, with the magnitude of the first peak decreasing with decreasing θ_R (Fig. 7b). This indicates that the in-plane ARF can be tuned by modulating θ_R. Moreover, when Y_{py} is positive, the entire cell experiences a force directed to the pressure nodes; otherwise, the force is directed to the pressure antinodes, a result with clear implications for SSAW-based microfluidics.

To establish how in-plane ARF can switch from attractive to repulsive, we plotted conditions and magnitudes for attractive (negative) ARF (Fig. 8, for the range $1 \leq f \leq 80$MHz and $1^\circ \leq \theta_R \leq 90^\circ$). Equilibrium positions for a cell can be tuned by changing the frequency f or the Rayleigh angle θ_R. This is further evident by plotting Y_{py} as a function of y_0 (Fig. 9a, for $\lambda_s = 100\ \mu$m), which shows that Y_{py} is a periodic function of period $\lambda_s/2$ due to the position-dependent term $\sin(2k_f y_0 \sin\theta_R) = \sin(2k_s y_0)$ in E_n, with amplitude changing depending upon θ_R. Plotting Y_{py} as a function of θ_R (Fig. 9b) further highlights the influence of Rayleigh angle, and again shows that Y_{py} increases with θ_R, which lead to more sound energy in y-direction. These results are meaningful in the design of microfluidics and highlight the critical role of Rayleigh angle in correctly predicting ARF. Again, we tested the effect of the constant $k_1 y_0$. For simplicity, the distance between the cell center to the antinode y_0 was fixed at $y_0 = 100\mu$m. We could also find that periodic peaks and dips would emerge as the $k_1 y_0$ increased. The reason is the same as the case for Fig. 5c.

To assess the role of cell and nucleus size on in-plane forces, we again varied cell radius r_1 while maintaining relative dimensions ($r_2 = 14r_1/15$ and $r_3 = 6r_1/15$, with $\theta_R = 80^\circ$ and $y_0 = \lambda_s/8$). As cell size increased, the Y_{py} peak shifted to a lower frequency, while the magnitude of this force peak remained constant (Fig. 10a). Cell size can affect the sign of Y_{py} so that cells will gather to the pressure antinode or the pressure node based on the cell size, suggesting a mechanism for acoustic cell sorting using SSAW. When plotted with nuclear and cortical dimensions held constant while cell volume changed, the Y_{py} peak shifted to a lower frequency and the force amplitude decreased (Fig. 10b). This was again expected because the cell nucleus size was different for the two cases in the two figures. The results shown in Fig. 10b also suggest that we can design SSAW based acoustic tweezers that sorting cells based on phase of the cell cycle.

5. Conclusions

We have shown that the design of SSAW microfluidic devices to manipulate cells is strongly dependent upon the Rayleigh angle of the system and the heterogeneous mechanics of the cells, neither of which had previously been explored theoretically. Our results extend the state of the art analysis to include waves other than plane standing waves, and to assess the effects of the Rayleigh angle and of cell mechanics. The theoretical model we derived reduced to earlier, simpler solutions for planar standing and planar traveling waves. It provided exact solutions for scattering coefficients, and a near-field approximation for the ARF.

These exact solutions have a number of limitations that bear mention. The first is that the mechanical properties of cells depend strongly upon the way that they are loaded (Elson and Genin, 2013; Marquez et al., 2005a; J.P. b; Rodriguez et al., 2013). The numbers used in the studies here are all derived from experiments that involve large perturbations of cells, but the application of ultrasound involves minimal deformation and relatively low stresses. The results presented may enable the estimation of mechanical properties at very low levels of cell deformation based upon motion in response to ARF. Second, the membrane of most cells is decorated with proteins that complicate the definition of a cortical layer thickness (Phillips et al., 2012). However, for most cells other than oocytes, the cortical layer is reduced in size in suspension and may not be a strong factor. Inside a tissue or a tissue construct, cells often surround themselves with a coating of extracellular matrix proteins that changes over time, even in cells that stay nominally round (Babaei et al., 2016a, 2016b; Guilak et al., 2018; Shakiba et al., 2020). This layer is typically much larger than the lipid membrane, in which case variations of the latter pose less of a concern.

Results show that consideration of the Rayleigh angle and cell mechanics are critical, and that these factors offer new handles with which to control cell manipulation and cell sorting. In the direction normal to the piezoelectric substrate, our model reveals that there is a non-zero component of the ARF that can be used to push a cell away or pull it back towards the sound source; prior theories fail to predict this phenomenon. The acoustic impedance mismatch between the cell nucleus and other cell components affects the ARF, as does the Rayleigh angle, the latter being a factor that can be tuned to switch ARF from attractive to repulsive. Within planes parallel to the piezoelectric substrate, the Rayleigh angle can be tuned to manipulate cells and sort them based upon size, mechanical properties, and phase within the cell cycle. Our model and results provide a theoretical foundation for harnessing the mechanical properties of cells to develop acoustic control for cell trapping, sorting, and manipulation.

Credit authorship contribution statement

Xiangjun Peng: Conceptualization, Methodology, Software, Validation, Investigation, Writing - original draft.
Wei He: Software, Validation.
Fengxian Xin: Writing - review & editing.
Guy M. Genin: Conceptualization, Methodology, Writing - review & editing, Supervision, Funding acquisition
Tian Jian Lu: Conceptualization, Methodology, Writing - review & editing, Supervision, Funding acquisition

Declaration of Competing Interest

The authors declare that they have no known competing financial interests or personal relationships that could have appeared to influence the work reported in this paper.

Acknowledgements

This work was supported in part by the National Natural Science Foundation of China (11972185), the Open Fund of the State Key Laboratory of Mechanics, and Control of Mechanical Structures of China (Grants MCMS-I-0219K01 and MCMS-E-0219K02), the China Scholarship Council (201906280470), and the National Institutes of Health (R01AR077793).

Appendix

The wave fields in cortical layer, cytoplasm, and cell nucleus can be explicitly expressed as a function of $X_n(\theta, \varphi; k_f y_0, \theta_R)$:

$$\begin{aligned} X_n\left(\theta,\varphi;k_f y_0,\theta_R\right) &= 2i^n(2n+1)\left(P_n(0)P_n(\cos\theta)\cos\left(k_f y_0\sin\theta_R\right)\right.\\ &+2\sum_{m=1}^{n}\frac{(n-m)!}{(n+m)!}P_n^m(0)P_n^m(\cos\theta)\left(\cos\left(k_f y_0\sin\theta_R\right)\cos m\varphi\cos m\theta_R\right.\\ &\left.\left.+i\sin\left(k_f y_0\sin\theta_R\right)\sin m\varphi\sin m\theta_R\right)\right) \end{aligned} \tag{25}$$

$$\phi_2 = \phi_0 e^{-i\omega t}\sum_{n=0}^{\infty}A_n j_n(k_2 r)X_n\left(\theta,\varphi;k_f y_0,\theta_R\right)$$

$$\phi_3 = \phi_0 e^{-i\omega t}\sum_{n=0}^{\infty}B_n j_n(k_3 r)X_n\left(\theta,\varphi;k_f y_0,\theta_R\right) \tag{26}$$

$$\phi_4 = \phi_0 e^{-i\omega t}\sum_{n=0}^{\infty}C_n j_n(k_4 r)X_n\left(\theta,\varphi;k_f y_0,\theta_R\right) \tag{27}$$

where A_n, B_n, and C_n are three different unknown coefficients describing the longitudinal wave, and $P_n^m(\cos\theta)$ denotes the associated Legendre polynomial. The remaining details of this derivation follow Liang (Liang et al., 2018a).

In the derivations of Eqs. (15) and (23), the following equations are adopted:

$$\int_0^{2\pi}\cos n\theta\cos m\theta\cos\theta d\theta = \begin{cases}\pi & (n+m=1)\\ \frac{\pi}{2} & \begin{pmatrix} n-m=\pm1\\ n\neq0,\ m\neq0\end{pmatrix}\\ 0 & \text{otherwise}\end{cases} \tag{28}$$

$$\int_0^{2\pi}\sin n\theta\sin m\theta\cos\theta d\theta = \begin{cases}\frac{\pi}{2} & \begin{pmatrix} n-m=\pm1\\ n\neq0,\ m\neq0\end{pmatrix}\\ 0 & \text{otherwise}\end{cases} \tag{29}$$

$$\int_0^{2\pi}\cos n\theta\sin m\theta\cos\theta d\theta = \begin{cases}0 & (n=1,\ m=0)\\ \pi & (n=0,\ m=1)\\ -\frac{\pi}{2} & (n-m=1,\ m\neq0)\\ \frac{\pi}{2} & (m-n=1,\ n\neq0)\\ 0 & \text{otherwise}\end{cases} \tag{30}$$

$$\int_0^{2\pi}\cos n\theta\cos m\theta\sin\theta d\theta = 0 \tag{31}$$

References

Azarpeyvand, M., Azarpeyvand, M., 2014. Application of acoustic bessel beams for handling of hollow porous spheres. Ultrasound Med. Biol. 40, 422–433.
Babaei, B., Davarian, A., Lee, S.-.L., Pryse, K.M., McConnaughey, W.B., Elson, E.L., Genin, G.M., 2016a. Remodeling by fibroblasts alters the rate-dependent mechanical properties of collagen. Acta Biomater. 37, 28–37.
Babaei, B., Davarian, A., Pryse, K.M., Elson, E.L., Genin, G.M., 2016b. Efficient and optimized identification of generalized Maxwell viscoelastic relaxation spectra. J Mech. Behav. Biomed. Mater. 55, 32–41.
Baddour, R.E., Kolios, M.C., 2007. The fluid and elastic nature of nucleated cells: implications from the cellular backscatter response. J. Acoustic. Soc. Am. 121, EL16–EL22.
Baddour, R.E., Sherar, M., Hunt, J., Czarnota, G., Kolios, M.C., 2005. High-frequency ultrasound scattering from microspheres and single cells. J. Acoust. Soc. Am. 117, 934–943.
Ding, X., Li, P., Lin, S.-C.S., Stratton, Z.S., Nama, N., Guo, F., Slotcavage, D., Mao, X., Shi, J., Costanzo, F., Huang, T.J., 2013. Surface acoustic wave microfluidics. Lab Chip 13, 3626–3649.
Dung Luong, T., Trung Nguyen, N., 2010. Surface acoustic wave driven microfluidics-a review. Micro Nanosyst. 2, 217–225.
Elson, E., Genin, G., 2013. The role of mechanics in actin stress fiber kinetics. Exp. Cell Res. 319, 2490–2500.

Faran, J.J., 1951. Sound scattering by solid cylinders and spheres. J. Acoust. Soc. Am. 23, 405–418.
Guilak, F., Nims, R.J., Dicks, A., Wu, C.-.L., Meulenbelt, I., 2018. Osteoarthritis as a disease of the cartilage pericellular matrix. Matrix Biol. 71, 40–50.
Guo, F., Li, P., French, J.B., Mao, Z., Zhao, H., Li, S., Nama, N., Fick, J.R., Benkovic, S.J., Huang, T.J., 2015. Controlling cell–cell interactions using surface acoustic waves. Proc. Natl. Acad. Sci. 112, 43–48.
Guo, F., Mao, Z., Chen, Y., Xie, Z., Lata, J.P., Li, P., Ren, L., Liu, J., Yang, J., Dao, M., 2016. Three-dimensional manipulation of single cells using surface acoustic waves. Proc. Natl. Acad. Sci. 113, 1522–1527.
Hasegawa, T., 1979. Acoustic radiation force on a sphere in a quasistationary wave field—Theory. J. Acoust. Soc. Am. 65, 32–40.
Hasegawa, T., Watanabe, Y., 1978. Acoustic radiation pressure on an absorbing sphere. J. Acoust. Soc. Am. 63, 1733–1737.
Hasegawa, T., Yosioka, K., 1969. Acoustic-radiation force on a solid elastic sphere. J. Acoust. Soc. Am. 46, 1139–1143.
Helgason, C.D., Miller, C.L., 2005. Basic Cell Culture Protocols. Humana Press, Totowa, NJ..
Holm, A., Stürzer, Q., Xu, Y., Weigel, R., 1996. Investigation of surface acoustic waves on LiNbO3, quartz, and LiTaO3 by laser probing. Microelectron. Eng. 31, 123–127.
Kim, M., Huff, E., Bottier, M., Dutcher, S.K., Bayly, P.V., Meacham, J.M., 2019. Acoustic trap-and-release for rapid assessment of cell motility. Soft Matter 15, 4266–4275.
King, L.V., 1934. On the acoustic radiation pressure on spheres. Proc. R. Soc. Lond. 147, 212–240.
Liang, S., Chaohui, W., Qiao, H., 2018a. Force on a compressible sphere and the resonance of a bubble in standing surface acoustic waves. Phys. Rev. E 98, 043108.
Liang, S., Chaohui, W., Qiao, H., 2018b. The radiation force on a rigid sphere in standing surface acoustic waves. J. Appl. Phys. 124, 104503.
Marquez, J.P., Genin, G.M., Zahalak, G.I., Elson, E.L., 2005a. The relationship between cell and tissue strain in three-dimensional bio-artificial tissues. Biophys. J. 88, 778–789.
Marquez, J.P., Genin, G.M., Zahalak, G.I., Elson, E.L., 2005b. Thin bio-artificial tissues in plane stress: the relationship between cell and tissue strain, and an improved constitutive model. Biophys. J. 88, 765–777.
Marston, P.L., 2006. Axial radiation force of a Bessel beam on a sphere and direction reversal of the force. J. Acoustic. Soc. Am. 120, 3518–3524.
Mishra, P., Hill, M., Glynne-Jones, P., 2014. Deformation of red blood cells using acoustic radiation forces. Biomicrofluidics 8, 034109.
Ozcelik, A., Rufo, J., Guo, F., Gu, Y., Li, P., Lata, J., Huang, T.J., 2018. Acoustic tweezers for the life sciences. Nat. Methods 15, 1021–1028.
Peng, X., He, W., Liu, Y., Xin, F., Lu, T.J., 2017. Optomechanical soft metamaterials. Acta Mech. Sinica 33, 575–584.
Peng, X., He, W., Xin, F., Genin, G.M., Lu, T.J., 2020. The acoustic radiation force of a focused ultrasound beam on a suspended eukaryotic cell. Ultrasonics 108, 106205.
Phillips, R., Kondev, J., Theriot, J., Garcia, H., 2012. Physical biology of the cell. Garland Sci..
Pratt, R.G., Simpson, G., Crossley, W.A., 1972. Acoustic-surface-wave properties of Bi12GeO20. Electron. Lett. 8, 127–128.
Rayleigh, L., 1902. On the pressure of vibrations. Philos. Mag. 3.
Rodriguez, M.L., McGarry, P.J., Sniadecki, N.J., 2013. Review on cell mechanics: experimental and modeling approaches. Appl. Mech. Rev. 65.
Shakiba, D., Alisafaei, F., Savadipour, A., Rowe, R.A., Liu, Z., Pryse, K.M., Shenoy, V.B., Elson, E.L., Genin, G.M., 2020. The balance between actomyosin contractility and microtubule polymerization regulates hierarchical protrusions that govern efficient fibroblast-collagen interactions. ACS Nano 14 (7), 7868–7869. doi:10.1021/acsnano.9b09941.
Wiklund, M., 2012. Acoustofluidics 12: biocompatibility and cell viability in microfluidic acoustic resonators. Lab Chip 12, 2018–2028.
Xu, S., Qiu, C., Liu, Z., 2012. Transversally stable acoustic pulling force produced by two crossed plane waves. EPL (Europhysics Letters) 99, 44003.
Yosioka, K., Kawasima, Y., 1955. Acoustic radiation pressure on a compressible sphere. Acta Acustica United with Acustica 5, 167–173 (167).
Zhang, G., Cui, J., 2018. Patch-clamp and perfusion techniques to study ion channels expressed in Xenopus oocytes. Cold Spring Harb. Protoc. 2018 pdb. prot099051.
Zhang, X., Zhang, G., 2012. Acoustic radiation force of a Gaussian beam incident on spherical particles in water. Ultrasound Med. Biol. 38, 2007–2017.